JGR Space Physics

RESEARCH ARTICLE
10.1029/2024JA032606

Quantifying the Role of EMIC Wave Scattering During the 27 February 2014 Storm by RAM-SCB Simulations

Xingzhi Lyu[1], Vania K. Jordanova[2], Miles Engel[2], Weichao Tu[1], and Qianli Ma[3,4]

[1]Department of Physics and Astronomy, West Virginia University, Morgantown, WV, USA, [2]Los Alamos National Laboratory, Los Alamos, NM, USA, [3]Department of Atmospheric and Oceanic Sciences, University of California, Los Angeles, Los Angeles, CA, USA, [4]Center for Space Physics, Boston University, Boston, MA, USA

Key Points:

- An updated RAM-SCB model is used to study the concurrent dropout of radiation belt (RB) electrons and ring current (RC) protons driven by EMIC wave scattering
- RAM-SCB simulations including Electromagnetic Ion Cyclotron wave scattering better capture the observed losses of both RB electrons and RC protons
- Simulated pitch angle distributions (PADs) of electrons peak at 90° with more losses at lower angles; protons show isotropic PADs with enhanced losses above 40°

Correspondence to:
X. Lyu,
xl0028@mix.wvu.edu

Citation:
Lyu, X., Jordanova, V. K., Engel, M., Tu, W., & Ma, Q. (2024). Quantifying the role of EMIC wave scattering during the 27 February 2014 storm by RAM-SCB simulations. *Journal of Geophysical Research: Space Physics*, *129*, e2024JA032606. https://doi.org/10.1029/2024JA032606

Received 4 MAR 2024
Accepted 1 JUL 2024

Abstract Electromagnetic Ion Cyclotron (EMIC) wave scattering has been proved to be responsible for the fast loss of both radiation belt (RB) electrons and ring current (RC) protons. However, its role in the concurrent dropout of these two co-located populations remains to be quantified. In this work, we study the effect of EMIC wave scattering on both populations during the 27 February 2014 storm by employing the global physics-based RAM-SCB model. Throughout this storm event, MeV RB electrons and 100s keV RC protons experienced simultaneous dropout following the occurrence of intense EMIC waves. By implementing data-driven initial and boundary conditions, we perform simulations for both populations through the interplay with EMIC waves and compare them against Van Allen Probes observations. The results indicate that by including EMIC wave scattering loss, especially by the He-band EMIC waves, the model aligns closely with data for both populations. Additionally, we investigate the simulated pitch angle distributions (PADs) for both populations. Including EMIC wave scattering in our model predicts a 90° peaked PAD for electrons with stronger losses at lower pitch angles, while protons exhibit an isotropic PAD with enhanced losses at pitch angles above 40°. Furthermore, our model predicts considerable precipitation of both particle populations, predominantly confined to the afternoon to midnight sector (12 hr < MLT < 24 hr) during the storm's main phase, corresponding closely with the presence of EMIC waves.

1. Introduction

The Earth's outer radiation belt consists of electrons with 100 s keV to multiple MeV energies and is characterized by large variations in electron flux on different time scales. The most dramatic variation is known as fast dropout, when the electron flux can drop by orders of magnitude within a few hours (e.g., Li et al., 2024; Onsager et al., 2002; Shprits et al., 2016; Tu et al., 2014; Xiang et al., 2017, 2018). Understanding where the electrons go during the dropout is one of the most important and compelling questions in the radiation belt studies. Recently, several papers have reported that these fast radiation belt (RB) electron dropouts are sometimes accompanied by the concurrent fast losses of 100s keV ring current (RC) protons (e.g., Gkioulidou et al., 2016; Lyu & Tu, 2022; Turner et al., 2014; Zhao et al., 2016). Previous studies on fast RB dropouts have shown that electrons can be lost through the magnetopause combined with outward radial diffusion (e.g., Olifer et al., 2019; Silva et al., 2022; Tu et al., 2019; Turner et al., 2012), or lost into the atmosphere due to the interaction with Electromagnetic Ion Cyclotron (EMIC) waves (e.g., Drozdov et al., 2020; Kersten et al., 2014; Ma et al., 2015; Ni et al., 2015; Zhang, Li, Ma, et al., 2016). Theoretically, both mechanisms are also efficient in driving the fast loss of energetic protons (at 100 s keV to MeV) in the ring current, which are collocated with RB electrons (e.g., Jordanova et al., 2001; Lyu, Tu et al., 2024; Lyu et al., 2022; Meredith et al., 2003). Therefore, a quantitative understanding of the coupling between the dropout of RB electrons and RC protons calls for more comprehensive data analysis as well as simulation efforts with physics-based models.

This work focuses on the latter loss mechanism, called EMIC wave scattering, which has been proven to be responsible for the fast losses of both particle populations (e.g., Blum et al., 2015; Cao et al., 2020; Jordanova et al., 2008). For example, Jordanova et al. (2003) simulated ring current evolution during the moderate storm of 10 January 1997 and found that EMIC waves were predominantly excited near Dst minimum on the duskside, where they caused strong ion precipitation consistent with Polar/IPS observations. Similarly, Jordanova et al. (2007) demonstrated that cyclotron resonant wave-particle interactions reproduced the proton precipitation during subauroral arc events observed with IMAGE/FUV imager and thus are a viable mechanism for the generation of subauroral proton arcs. For radiation belt electrons, Li et al. (2014) analyzed and simulated a

relativistic electron precipitation event on 17 March 2013 observed by the Balloon Array for Radiation belt Relativistic Electron Losses (BARREL) during a period of strong EMIC wave activities. Their results suggested that the observed electron precipitation is likely caused by EMIC wave scattering. For ring current protons, Usanova et al. (2010) conducted an analysis of EMIC wave excitation during a storm event, utilizing ground-based and multi-satellite measurements. Their findings revealed that EMIC waves can be effective in causing localized precipitation of protons with energies above 30 keV. A few detailed event studies have also been performed in comparing the dropout of RB electrons with the loss of RC protons (e.g., Cao et al., 2019; Engebretson et al., 2015; Lyu et al., 2022; Miyoshi et al., 2008; Ni et al., 2023). For example, Capannolo et al. (2019) reported the concurrent precipitations of 10–100 s keV protons and relativistic electrons driven by EMIC waves during three storm events based on the measurements of multiple Low-Earth-Orbiting (LEO) Polar Operational Environmental Satellites/Meteorological Operational satellite program (POES/MetOp) satellites. Jordanova et al. (2008) modeled the coupling between 100 keV ring current protons and MeV radiation belt electrons through the interplay with EMIC waves. Their results show enhanced proton precipitation by EMIC waves concurrent with precipitation of relativistic electrons, even though the work primarily focused on RB dropout without delving into the consequent proton dropout.

As the previous works discussed above are either qualitative or just focus on one population, a comprehensive comparative study is needed to determine quantitatively the role of EMIC wave scattering to the concurrent dropout of both populations. Therefore, in our recent work (Lyu et al., 2022) we modeled the simultaneous dropout of MeV electrons and 100s keV protons observed by Van Allen Probes on 27 February 2014. By implementing a 2-D pitch angle and energy diffusion model with event-specific diffusion coefficients, the evolution of pitch angle distributions is simulated for both populations at a specific location (L ~ 5.2), where the most intense EMIC waves are observed. The results indicate that EMIC wave scattering can efficiently cause the simultaneous depletion of both energetic electrons and protons on a timescale of ~40 min. However, even though this study reveals the important role of EMIC wave scattering in the concurrent localized dropout of both populations, it only focused on one L shell and was based on a drift-averaged model without a local time dependence. The relative contribution of EMIC wave scattering to the global variations of both RB electrons and RC protons still remains to be quantified. Thus, in this work, we simulate the 27 February 2014 storm event by employing the global kinetic Ring current–Atmosphere interactions Model (RAM) coupled with a three-dimensional (3-D) Self-Consistent magnetic (B) field code (SCB). By implementing a more recent statistical EMIC wave model from Van Allen Probes observation (Zhang, Li, Thorne, et al., 2016), we quantitatively study the coupling of the dropout between MeV RB electrons and 100s keV RC protons by the interplay with EMIC waves.

2. Model Description

RAM-SCB is a model that combines a kinetic model of ring current plasma (e.g., Jordanova et al., 2001, 2010) with a 3-D force balanced model of the terrestrial magnetic field (e.g., Engel et al., 2019; Zaharia et al., 2006). Over the past decade, this model has been successfully applied to many inner magnetospheric studies (e.g., Jordanova et al., 2003, 2016; Welling et al., 2011). In particular, Jordanova and Miyoshi (2005) first extended the global RAM to relativistic energies and electrons, which enables the study on radiation belt dynamics as well as its coupling with ring current variations. In the relativistic case, the RAM module numerically solves the kinetic equation for the bounce-averaged distribution function of particles, as:

$$\frac{\partial Q_l}{\partial t}+\frac{1}{R_0^2}\frac{\partial}{\partial R_0}\left(R_0^2\left\langle\frac{dR_0}{dt}\right\rangle Q_l\right)+\frac{\partial}{\partial \phi}\left(\left\langle\frac{d\phi}{dt}\right\rangle Q_l\right)+\frac{1}{\gamma p}\frac{\partial}{\partial E}\left(\gamma p\left\langle\frac{dE}{dt}\right\rangle Q_l\right)+\frac{1}{h\mu_0}\frac{\partial}{\mu_0}\left(h\mu_0\left\langle\frac{d\mu_0}{dt}\right\rangle Q_l\right)$$
$$=\left\langle\left(\frac{\partial Q_l}{\partial t}\right)_{loss}\right\rangle \quad (1)$$

where $Q_l(R_0, \phi, E, \mu_0, t)$ is the phase space distribution function of species l as a function of radial distance in the magnetic equatorial plane R_0, geomagnetic east longitude ϕ, particle kinetic energy E, equatorial pitch angle α_0 (with $\mu = \cos(\alpha_0)$), and time t; p is the relativistic momentum of the particle and γ is the relativistic factor; $h = 1/(2R_0)\int_{s_{m1}}^{s_{m2}} ds/\sqrt{(1-B(s)/B_m)}$ is calculated for the realistic B field along the field line between the mirror points s_{m1} and s_{m2}; the angle brackets denote bounce-averaging; and the subscript "0" refers to the quantities in the magnetic equatorial plane. The model domain in this study covers R_0 from 2 to 6.5 R_E and all magnetic local times

(MLT). It includes RC ions (H^+, He^+, O^+) with energies from 0.1 to 500 keV, RB electrons with energies from 10 keV expanded to 8 MeV, and α_0 from 0° to 90°. The left-hand side of Equation 1 describes the transport and acceleration of charged particles along adiabatic drift paths in time-dependent electric and magnetic fields. The right-hand side describes changes of Q_l due to various loss processes. For ring current ions, the loss processes included in this paper are charge exchange, wave particle interactions with EMIC waves, and loss to the atmosphere (due to the emptying of the loss cone). For radiation belt electrons, the loss processes consist of wave particle interactions with plasmaspheric hiss and whistler mode chorus using electron lifetimes and scattering by EMIC waves using quasi-linear diffusion coefficients which will be explained below, and loss to the atmosphere. The electric field used in this study is from the Weimer (2005) model, while the self-consistent magnetic field is updated every 5 min by solving the single-fluid plasma force balance equation.

Electron fluxes measured by the Magnetic Electron Ion Spectrometer (MagEIS) (Blake et al., 2013) and Relativistic Electron Proton Telescope (REPT) instruments (Baker et al., 2013) onboard Van Allen Probes are used in this study. The proton data are provided by the Helium Oxygen Proton Electron mass spectrometer (HOPE) (Funsten et al., 2013) and the Radiation Belt Storm Probes Ion Composition Experiment (RBSPICE) instruments (Mitchell et al., 2013). The model initial conditions for both populations are derived based on quiet time measurements (one day before the simulation interval, specifically from 12 UT on 02/26 to 12 UT on 02/27, 2014) which illustrate weak MLT dependence. Thus, the initial distributions are assumed to be uniform throughout all MLT. The nightside boundary conditions are determined from plasma sheet flux measurements from the Magnetospheric Plasma Analyzer (MPA) and Synchronous Orbit Particle Analyzer (SOPA) instruments on the LANL geosynchronous spacecraft as in our previous studies (e.g., Jordanova et al., 2007).

To implement pitch angle scattering by EMIC waves in this study, we use a recent statistical EMIC wave model by Zhang, Li, Thorne, et al. (2016), which is constructed based on more than 3 years' Van Allen Probes measurements. The spatial distribution of the EMIC wave amplitudes are categorized into three AL^* (defined as the minimum AL index in the preceding 3 hr) levels (i.e., quiet time: $AL^* > -250$ nT; moderate storm time: -650 nT $< AL^* < -250$ nT; disturbed time: $AL^* < -650$ nT) in both the H^+ and He^+ frequency bands. The statistical distribution of the EMIC wave frequency spectra for different ranges of f_{pe}/f_{ce} (including $f_{pe}/f_{ce} < 5$, $5 < f_{pe}/f_{ce} < 15$, and $f_{pe}/f_{ce} > 15$) are also reported in their study, which is also implemented in our model. We calculate the EMIC wave diffusion coefficients based on the quasi-linear theory using the full diffusion code (Ma et al., 2019), considering the statistical EMIC wave frequency spectra and wave amplitude at each L shell and MLT. Because we only consider the left-hand polarized EMIC waves, the wave power spectral densities in the stop band (Albert, 2003) are excluded. In addition, the latitude range of EMIC wave is assumed to be from the equator to the latitude where the wave polarization changes from left-hand to right-hand polarized (i.e., the wave frequency reaches the crossover frequency). We assume an ion composition ratio of H^+: He^+: $O^+ = 90\%$: 5%: 5% following Blum et al. (2019). We use the latitudinally-varying wave normal angle distribution from Ni et al. (2015), which is field-aligned near the equator and more oblique at higher latitudes. The calculation is performed using both the plasmaspheric density and plasma trough density from Sheeley et al. (2001) and the density is assumed to be constant along the field line. The diffusion coefficients due to EMIC waves outside or inside the plasmapause are incorporated in the RAM-SCB model based on the simulated plasmapause location.

3. Simulation Results

3.1. Simulations of Omni-Directional Fluxes

Figure 1 shows the observed and simulated omni-directional electron fluxes along the orbit of Van Allen Probe B from 12 UT on February 27 to 12 UT on 28 February 2014, accompanied by the SYM-H index at the bottom panel. Figure 1a shows the electron flux data as a function of time and energy from ~100 keV to 8 MeV, while the simulated electron fluxes by our model are shown in panels b and c. To provide a more detailed comparison between data and model, panel d displays observed and modeled electron fluxes at a given energy of 900 keV, with black being the data and blue and red being the model results. The observations show that MeV electron fluxes experience a significant decrease during both the main and recovery phases of the storm (after ~ 19 UT on February 27), which is particularly evident in the black line in panel d. For the simulations of electrons, we first incorporated loss mechanisms within the plasmasphere due to hiss waves (Albert, 1999) and outside the plasmasphere resulting from chorus wave scattering (for further details, see Jordanova et al., 2008, 2010, and references therein), treating them as the major default loss factors for RB electrons at energies below a few hundred

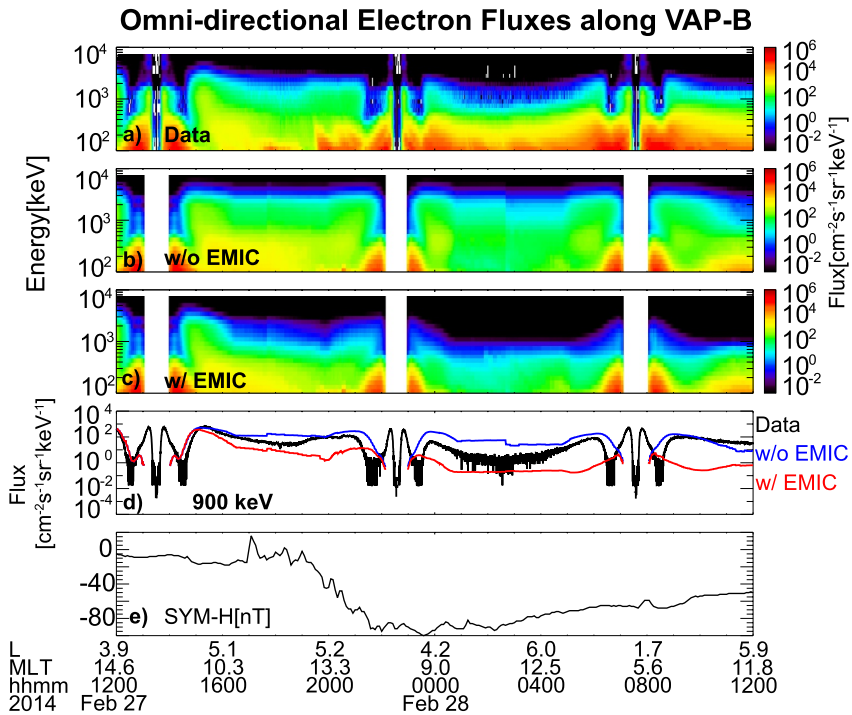

Figure 1. (a–c) Observed and simulated omni-directional electron fluxes (normalized per steradian) from 12 UT on February 27 to 12 UT on 28 February 2014, along Van Allen Probe B's orbit. (d) Comparison between observed 900 keV electron flux data (in black) and RAM-SCB simulations without (in blue) and with (in red) including the loss induced by EMIC wave scattering. (e) SYM-H index.

keV. Model results with these loss processes are shown in panel b and as the blue curve in panel d. Subsequently, the role of EMIC wave scattering in the observed electron losses are investigated by further adding in the Helium band (He-band) and Hydrogen band (H-band) EMIC waves in the model, with results shown in panel c and as the red curve in panel d. By comparing our RAM-SCB simulations with data, we note that the model results without including EMIC waves (Figure 1b) underestimate the observed MeV electron losses. This underestimation is distinct in panel d, where the blue line, representing the simulated 900 keV electron fluxes, consistently exceeds the observational data (black line) throughout both the storm's main phase and the subsequent recovery phase. After incorporating the EMIC wave scattering effect, as shown in Figure 1c and the red line in panel d, our model produces significant losses of radiation belt electrons with slight overestimations of the flux loss compared to data.

Figure 2a illustrates the observed proton fluxes as a function of energy from 50 to 450 keV, while the simulated fluxes without and with including EMIC waves are shown in Figures 2b and 2c, respectively. The observed and modeled 270 keV proton fluxes are plotted in panel d for a more detailed comparison. The data indicates that 100s keV proton fluxes experience a simultaneous dropout with MeV RB electrons during the storm time, as shown by both Figure 2a and the black line in Figure 2d. For the simulations, the primary mechanism for the loss of ring current protons we first include in the model is charge exchange. Similar to the findings for electrons, the comparison between data and model results reveals that simulation without including EMIC waves underestimates the observed losses of 100s keV protons during both the storm main and recovery phases, as depicted in Figure 2b and the blue line in panel d. However, the model that includes the EMIC wave scattering effect, as shown in panel c and the red line in panel d, better captures the observed 100s keV proton losses.

The data-model comparison along Van Allen Probe B's orbit shown in Figures 1 and 2 have suggested the importance of EMIC wave scattering in reproducing the concurrent dropout of both populations. Notably, the same comparison along Probe A's orbit (not shown) was also performed and yielded similar conclusions. Furthermore, by comparing to the data our model can be used to investigate which band of the EMIC waves are more dominant during this storm-time dropout event. Figure 3 illustrates the drift and bounce-averaged pitch

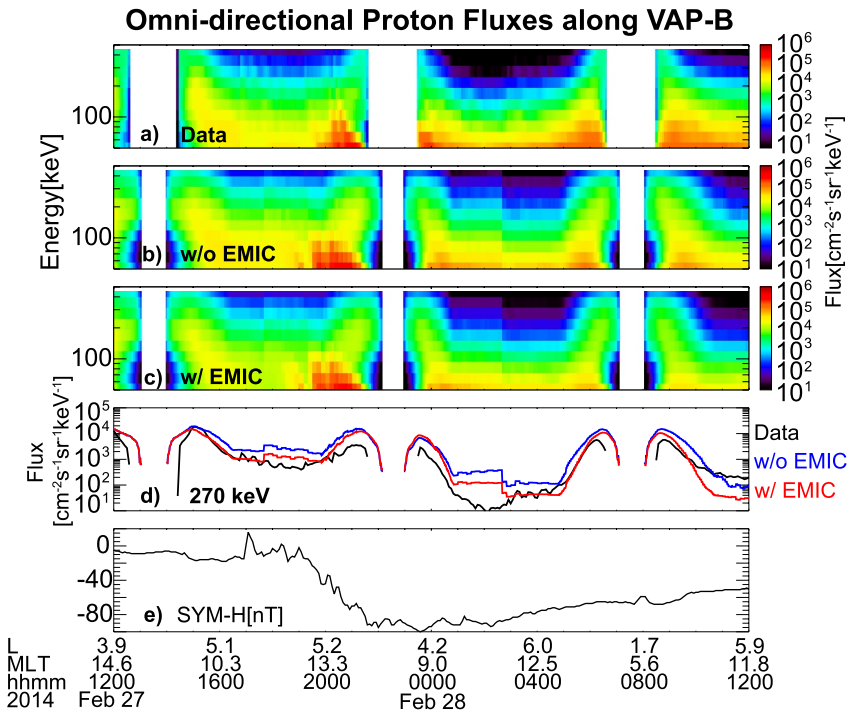

Figure 2. Observed and simulated omni-directional proton fluxes (normalized per steradian) in the same format as Figure 1.

angle diffusion coefficients calculated based on the statistical wave model (Zhang, Li, Thorne, et al., 2016) for both electrons (first row) and protons (second row) at $L = 5.2$ and 20 UT of 27 February 2014, when intense EMIC waves were observed by Van Allen Probes (Lyu et al., 2022). The diffusion rates driven by H-band EMIC waves (panels a and c) and He-band EMIC waves (panels b and d) are plotted against equatorial pitch angle and energy for both populations. H-band EMIC waves are found to effectively scatter electrons above 600 keV, while He-band waves exhibit a higher efficiency for >4 MeV electrons. For ring current protons, the resonant

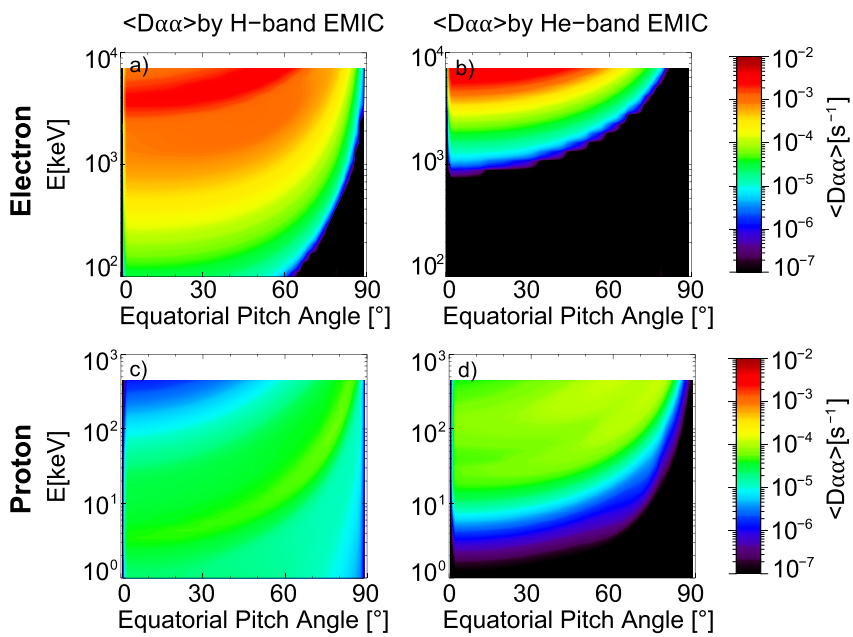

Figure 3. Drift averaged $<D_{\alpha\alpha}>$ of electrons (panels a and b) and protons (panels c and d) by different bands of EMIC waves (Hydrogen band on the left, Helium band on the right) at $L = 5.2$ and 20 UT of 27 February 2014.

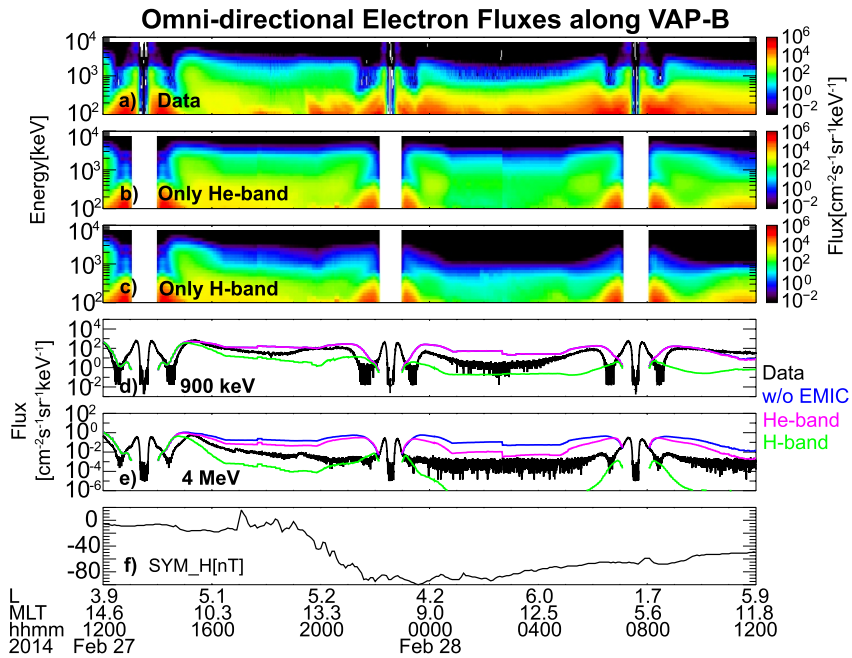

Figure 4. (a) Observed electron omni-directional flux (normalized per steradian), same plot as Figure 1a. Simulated electron flux by including the loss driven by (b) only He-band EMIC waves and (c) H-band EMIC waves, respectively. Comparison between the observed (d) 900 keV and (e) 4 MeV electron flux data (in black) and RAM-SCB simulations without including EMIC wave scattering loss (blue), only including the scattering loss by He-band EMIC waves (magenta), and only including the loss driven by H-band EMIC waves (green). (f) SYM-H index.

interactions with H-band EMIC waves primarily occur at lower energies (~10s keV), whereas He-band EMIC waves have a more significant impact on scattering 100s keV protons.

By implementing these diffusion coefficients driven by different bands of EMIC waves in our simulation, Figures 4a–4c compare the energy spectrum of the observed (panel a) and modeled omni-directional electron fluxes by including only He-band (panel b) or H-band (panel c) EMIC waves. Panels d and e directly compare the electron flux observations (black line) against simulation results at two different electron energies, 900 keV and 4 MeV: without EMIC waves (blue line), with only He-band EMIC waves (magenta line), and with only H-band EMIC waves (green line). For electrons, the results show that our model with including only He-band EMIC waves well captures the observed electron losses at > 3 MeV during both the storm main and recovery phases, as depicted in Figure 4b and represented by the magenta line in Figure 4e. For <3 MeV electrons, including only He-band EMIC waves are less efficient in capturing the observed losses, as the magenta line overlaps with the blue line in Figure 4d. On the other hand, the simulations with only H-band EMIC waves (Figure 4c) reproduced the observed loss of electrons below 1 MeV (shown from Figure 4d), but significantly overestimated the electron losses at energies above 1 MeV (e.g., comparing the black and the green lines in Figure 4e). These are consistent with the energy coverage and dependence of the electron pitch angle diffusion coefficients due to H-band and He-band EMIC waves shown in the top row of Figure 3.

The same energy spectrum plots for the observations and simulations of ring current protons are shown in Figures 5a–5c. Panel d illustrates the observed and modeled 270 keV proton fluxes in line plots for a detailed comparison. For 100s keV protons, the model results including only H-band EMIC waves (Figure 5c and green line in Figure 5d) only show a very small difference compared to those without including EMIC waves (Figure 2b and blue line in Figure 5d), both of which underestimate the observed losses. This suggests that H-band EMIC waves have very limited contribution to the loss of 100s keV protons during this event. However, the simulation with only He-band EMIC waves shown in Figure 5b and the magenta line in Figure 5d aligns better with the data (Figure 5a and black line in Figure 5d). This suggests that He-band EMIC waves play a dominant role in driving the observed 100s keV proton losses. To summarize, our simulation results indicate that the simultaneous dropout of radiation belt electrons at >1 MeV and 100s keV ring current protons during this event can largely be attributed

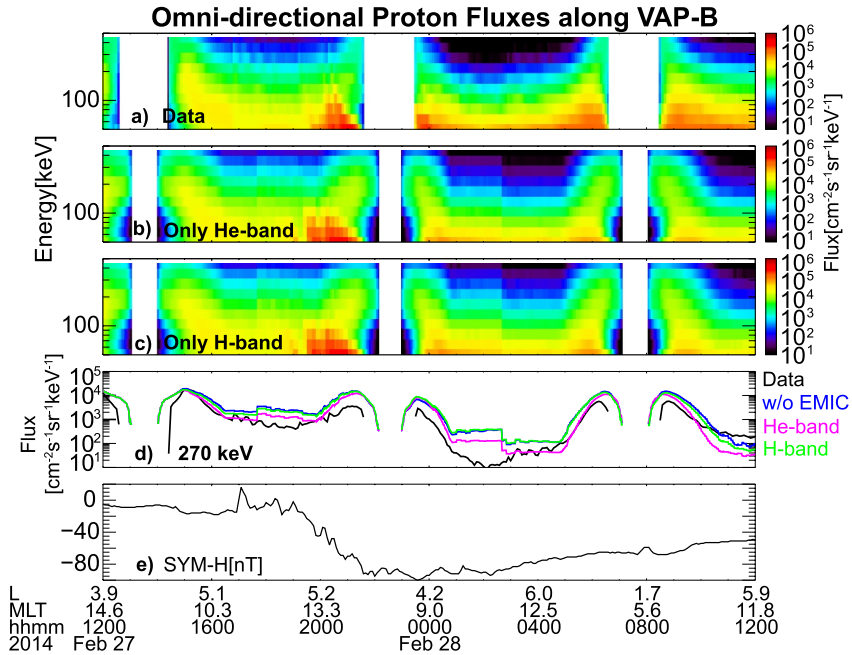

Figure 5. Observed and simulated proton omni-directional fluxes (normalized per steradian) in the same format as Figure 4.

to He-band EMIC waves. The simulations with only H-band EMIC waves dominate the loss of electrons <1 MeV but overestimate the MeV electron losses and show less efficiency in scattering 100s keV protons.

3.2. Simulations of Pitch Angle Distributions

Based on the diffusion coefficients by both H-band and He-Band EMIC waves displayed in Figure 3, we further investigate the evolution of the simulated pitch angle distributions for both populations. The initial distributions plotted as solid lines in Figure 6 are derived from our data-driven initial conditions at $L = 5.2$ and 1200 UT on 27

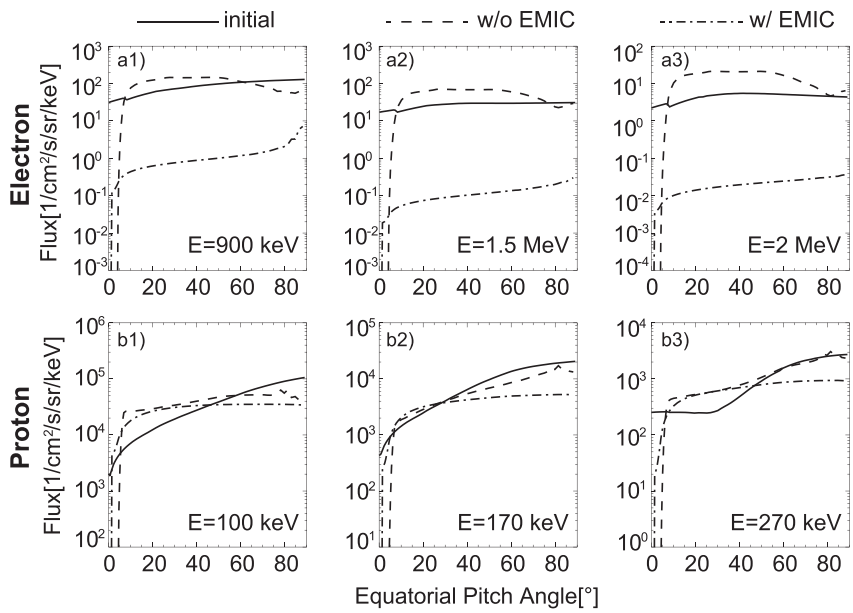

Figure 6. Calculated relativistic electron (panels a1–a3) and ring current proton (panels b1–b3) fluxes at three energies and $L = 5.2$ and MLT = 1300, where the initial pitch angle distributions (PADs) are shown as the solid lines, simulated PADs without EMIC wave scattering in dashed lines, and with EMIC wave scattering in dashed-dotted lines.

February. To isolate the effects of EMIC waves, Figure 6 presents the fluxes of electrons (top) and protons (bottom) at the same L shell, MLT = 13 hr, and time (20 UT on 27 February), across various energies as a function of equatorial pitch angle, without (dashed) and with (dashed-dotted) including EMIC wave scattering in the model. For electrons, in Figures 6a1–6a3, the loss from the initials (solid lines) to the distributions with including EMIC waves (dashed-dotted lines) gets stronger at higher electron energies. This trend aligns with the energy dependence of the diffusion rates presented in Figures 3a and 3b. Comparing the simulated fluxes along pitch angles, the inclusion of EMIC waves in the model leads to a 90° peaked PAD with faster losses at lower pitch angles, which is also consistent with the pitch angle dependence of the electron diffusion coefficients shown in Figures 3a and 3b. However, for 100s keV proton fluxes shown in Figures 6b1–6b3, the losses from initials (solid lines) to EMIC-influenced distributions (dashed-dotted lines) does not show strong energy dependence, which agree with the energy dependence of diffusion coefficients shown in Figure 3d for He-band EMIC waves which dominate the diffusion rates. Comparing the simulations without (dashed lines) and with (dashed-dotted lines) including EMIC waves against the initials (solid lines), protons with EMIC wave scattering exhibit a more isotropic PAD with more pronounced scattering at pitch angles above 40°.

3.3. Global Distribution of Precipitating Fluxes

Energetic particles scattered by the interaction with EMIC waves into the loss cone are precipitated into the dense atmosphere. Figure 7a shows the AL index during our simulation interval. Based on the statistical EMIC wave model outlined in Section 2, we select the time of 2300 UT on 27 February, when AL drops to its minimum (∼−800 nT) during the storm main phase, for the detailed investigation of the global distributions of EMIC wave amplitudes (Figures 7b and 7c), pitch angle diffusion coefficients (Figures 7d and 7e), and precipitating electron and proton fluxes (Figures 7f and 7g). Under the very disturbed geomagnetic conditions ($AL^* \leq -800$ nT), strong H-band and He-band EMIC waves are mostly confined to the afternoon sector (12 hr < MLT < 18 hr), as well as the nightside sector (18 hr < MLT < 24 hr) located closer to the Earth (Zhang, Li, Thorne, et al., 2016). The pitch angle diffusion coefficients combining the effects of both H-band and He-band EMIC waves are shown in Figures 7d and 7e for 1 MeV electrons and 100 keV protons respectively. Stronger diffusion rates are shown to locate at L shells between 4 and 6.5 in the afternoon sector for both populations. There are also some high diffusion rates distributed at L < 3.5 for 1 MeV electrons near the nightside. With EMIC wave scattering effects included in our model, we calculate the precipitating fluxes defined as the fluxes at the edge of the loss cone for both populations. The loss cone in our model corresponds to particles mirroring at 200 km altitude in the atmosphere, that is, equatorial pitch angle of ∼3° at $L = 6$, increasing to ∼17° at $L = 2$ (Jordanova et al., 2008). As shown in Figures 7f and 7g, considerable precipitating fluxes for both populations are predicted by the model and are predominantly concentrated in the afternoon to midnight sector, which corresponds closely with the distributions of EMIC waves in both radial distance and MLT.

4. Summary and Conclusions

Simultaneous dropout of both MeV radiation belt electrons and 100s keV ring current protons is observed by Van Allen Probes during the 27 February 2014 geomagnetic storm, accompanied by intense EMIC wave activities (Lyu et al., 2022; Xiang et al., 2017; Zhang, Li, Ma, et al., 2016). To quantitatively study the role of EMIC wave scattering in the concurrent dropout of both populations using RAM-SCB simulations, a statistical EMIC wave model depending on the geomagnetic conditions by Zhang, Li, Thorne, et al. (2016) is implemented to simulate the EMIC wave activity and calculate the pitch angle diffusion coefficients as the input for RAM-SCB to compute the scattering losses for both particle populations. The initial conditions for both electrons and protons were derived from the Van Allen Probes measurements, while the time-varying geosynchronous data from LANL satellites were used at the outer boundary. The RAM model includes both convective and radial transport and various loss processes (major loss: hiss inside plasmapause and chorus outside plasmapause for electrons; charge exchange for protons). To differentiate EMIC wave associated loss, we performed simulations without and with including EMIC waves (while keeping all the other processes) and compared the simulation results with observations. Further investigations on which band of EMIC waves is more dominant during this storm event for both populations were conducted. Additionally, we investigated the evolution of the pitch angle distributions (PADs) and the global distributions of precipitating fluxes for both populations due to EMIC wave scattering. Our major findings are summarized in the following:

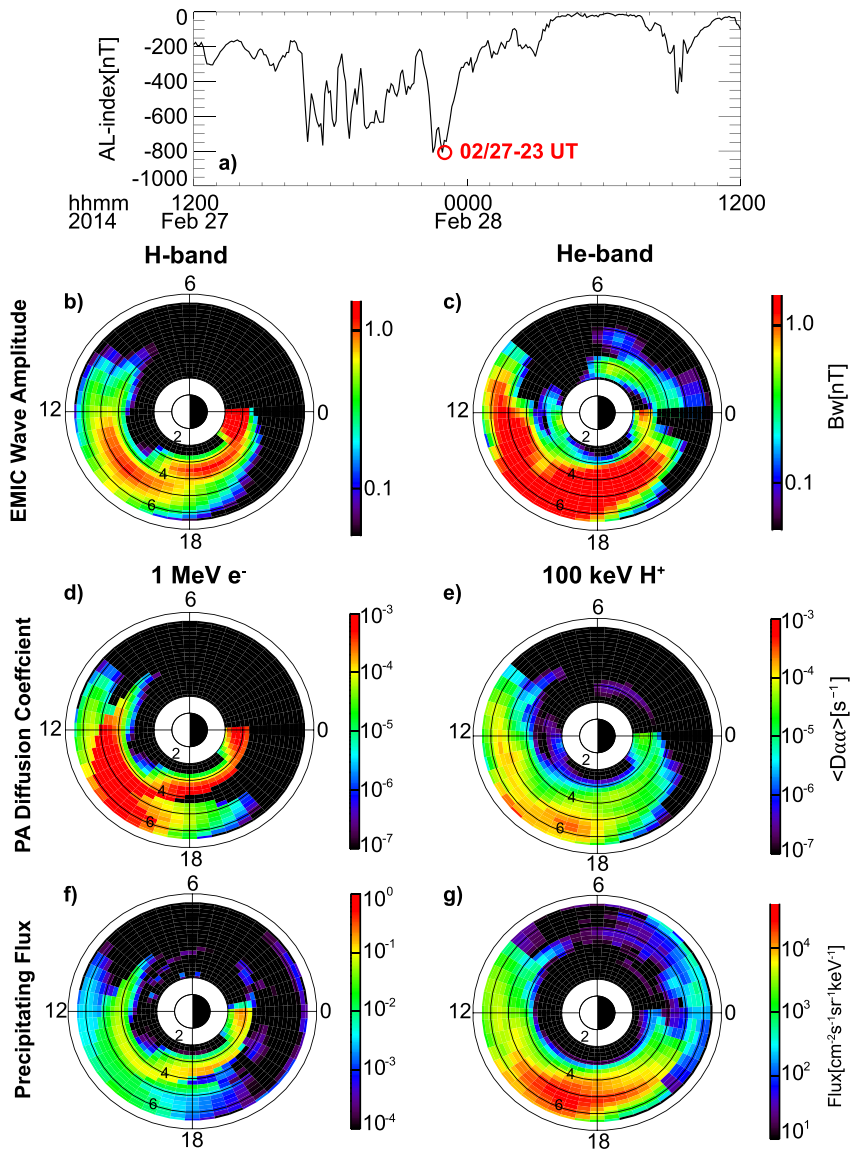

Figure 7. (a) AL-index from 02/27-12 UT to 02/28-12 UT, 2014. (b–c) H-band and He-band EMIC wave amplitudes under the disturbed conditions ($AL^* < -650$ nT) based on the statistical wave model by Zhang, Li, Ma, et al. (2016). (d–e) Global distributions of the calculated bounce-averaged pitch angle diffusion coefficients (at ~10°, near the edge of the loss cone) for (d) 1 MeV electrons and (e) 100 keV protons at 23 UT on February 27. (f–g) The corresponding global precipitating flux distributions of (f) 1 MeV electrons and (g) 100 keV protons.

1. The comparison between the simulations without and with EMIC waves against data indicate that the model including EMIC wave scattering better captures the observed concurrent dropouts of MeV radiation belt electrons and 100s keV ring current protons during the storm main phase, although there is some slight overestimation of the electron losses. This overestimation could potentially be due to the uncertainties in the empirical EMIC wave model.
2. By including only H-band or He-band EMIC waves in the simulations, we found the concurrent dropout between >1 MeV electrons and 100s keV protons are largely caused by the He-band EMIC waves. Conversely, simulations that only include H-band EMIC waves well capture the <1 MeV electron losses, but overestimate MeV electrons losses and are less efficient in capturing the losses of 100s keV protons. To fully resolve the contribution of different bands of EMIC waves during this event, event-specific and global observations rather than empirical models of EMIC waves in H-band and He-band are required.

3. The study investigates the evolution of simulated pitch angle distributions (PADs) at $L = 5.2$ and MLT = 1300 for MeV electrons and 100 keV protons. For MeV electrons, it is found that losses are more significant at higher energies and pitch angles <70°, resulting in a PAD that is more peaked around 90°. In contrast, for 100 keV protons, the energy dependence of losses is less pronounced compared to electrons. The PAD for protons becomes more isotropic due to faster losses at pitch angles above 40°.
4. Under very disturbed geomagnetic conditions (AL ≤ −800 nT), global distributions of the precipitating fluxes for both populations are predominantly confined to the afternoon to midnight sector (12 hr < MLT < 24 hr), which closely corresponds to the presence of the EMIC waves in space.

In conclusion, this study demonstrated the importance of EMIC wave scattering in reproducing the concurrent dropout of MeV radiation belt electrons and 100 s keV ring current protons during the February 2014 storm event through our updated RAM model coupled with the self-consistent magnetic field model (SCB). In the modeling, we used statistical models of EMIC wave amplitudes, frequency spectra, and total electron density, and made assumptions on the wave normal angle and ion composition. The simulation results may be sensitive to these parameters. For example, Yue et al. (2023) provided the ion composition ratios at different L and MLT using the Van Allen Probes statistics. We plan to evaluate the main parameters and factors affecting the electron and proton loss rates and dropouts in future extensions of this work. It is also important to note that the potential contribution of field line curvature (FLC) scattering, cannot be ruled out for this event since it could also cause the precipitation loss of both radiation belt electrons and ring current protons (e.g., Artemyev et al., 2013; Cao et al., 2023). But it is beyond the scope of this work, and we plan to include the FLC effects in the future.

Data Availability Statement

We acknowledge the Van Allen Probes data from MagEIS and REPT instrument, as well as the MagEphem data obtained from https://rbsp-ect.newmexicoconsortium.org/science/DataDirectories.php, RBSPICE instrument obtained from http://rbspice.ftecs.com/Data.html. RAM-SCB code is publicly available at https://github.com/lanl/RAM-SCB. The model inputs and outputs used in this study are publicly available at Zenodo (Lyu, Jordanova, et al., 2024).

Acknowledgments
This work was supported by NASA Grants 80NSSC19K0908, 80NSSC21K1312, and 80NSSC21K2008, and NSF Grants AGS 1752736 and AGS-2247856. QM would like to acknowledge the NASA Grants 80NSSC20K0196 and 80NSSC24K0572, and NSF Grant AGS-2225445. Work at Los Alamos was performed under the auspices of the U.S. Department of Energy (Contract No. 89233218CNA000001) and was partially funded by NASA Grants 80HQTR21T0115, 80HQTR21T0008, and NSF Grant IAA2027951.

References

Albert, J. M. (1999). Analysis of quasi-linear diffusion coefficients. *Journal of Geophysical Research*, *104*(A2), 2429–2441. https://doi.org/10.1029/1998JA900113

Albert, J. M. (2003). Evaluation of quasi-linear diffusion coefficients for EMIC waves in a multispecies plasma. *Journal of Geophysical Research*, *108*(A6), 1249. https://doi.org/10.1029/2002JA009792

Artemyev, A. V., Orlova, K. G., Mourenas, D., Agapitov, O. V., & Krasnoselskikh, V. V. (2013). Electron pitch-angle diffusion: Resonant scattering by waves vs. nonadiabatic effects. *Annals of Geophysics*, *31*(9), 1485–1490. https://doi.org/10.5194/angeo-31-1485-2013

Baker, D. N., Kanekal, S. G., Hoxie, V. C., Batiste, S., Bolton, M., Li, X., et al. (2013). The relativistic electron-proton telescope (REPT) instrument on board the radiation belt storm probes (RBSP) spacecraft: Characterization of Earth's radiation belt high-energy particle populations. *Space Science Reviews*, *179*(1–4), 337–381. https://doi.org/10.1007/s11214-012-9950-9

Blake, J. B., Carranza, P. A., Claudepierre, S. G., Clemmons, J. H., Crain, W. R., Jr., Dotan, Y., et al. (2013). The magnetic electron ion spectrometer (MagEIS) instruments aboard the radiation belt storm probes (RBSP) spacecraft. *Space Science Reviews*, *179*(1–4), 383–421. https://doi.org/10.1007/s11214-013-9991-8

Blum, L. W., Artemyev, A., Agapitov, O., Mourenas, D., Boardsen, S., & Schiller, Q. (2019). EMIC wave-driven bounce resonance scattering of energetic electrons in the inner magnetosphere. *Journal of Geophysical Research: Space Physics*, *124*(4), 2484–2496. https://doi.org/10.1029/2018JA026427

Blum, L. W., Halford, A., Millan, R., Bonnell, J. W., Goldstein, J., Usanova, M., et al. (2015). Observations of coincident EMIC wave activity and duskside energetic electron precipitation on 18–19 January 2013. *Geophysical Research Letters*, *42*(14), 5727–5735. https://doi.org/10.1002/2015GL065245

Cao, X., Ni, B., Summers, D., Shprits, Y. Y., Gu, X., Fu, S., et al. (2019). Sensitivity of EMIC wave-driven scattering loss of ring current protons to wave normal angle distribution. *Geophysical Research Letters*, *46*(2), 590–598. https://doi.org/10.1029/2018GL081550

Cao, X., Ni, B., Summers, D., Shprits, Y. Y., & Lou, Y. (2020). Effects of polarization reversal on the pitch angle scattering of radiation belt electrons and ring current protons by EMIC waves. *Geophysical Research Letters*, *47*(17), e2020GL089718. https://doi.org/10.1029/2020GL089718

Cao, X., Ni, B., Yu, Y., Ma, L., Lu, P., & Wang, X. (2023). Comparison of ring current proton losses between contributions from scattering by field line curvature and EMIC waves. *Journal of Geophysical Research: Space Physics*, *128*(12), e2023JA031904. https://doi.org/10.1029/2023JA031904

Capannolo, L., Li, W., Ma, Q., Shen, X.-C., Zhang, X.-J., Redmon, R. J., et al. (2019). Energetic electron precipitation: Multievent analysis of its spatial extent during EMIC wave activity. *Journal of Geophysical Research: Space Physics*, *124*(4), 2466–2483. https://doi.org/10.1029/2018JA026291

Drozdov, A. Y., Usanova, M. E., Hudson, M. K., Allison, H. J., & Shprits, Y. Y. (2020). The role of hiss, chorus, and EMIC waves in the modeling of the dynamics of the multi-MeV radiation belt electrons. *Journal of Geophysical Research: Space Physics*, *125*(9), e2020JA028282. https://doi.org/10.1029/2020JA028282

Engebretson, M. J., Posch, J. L., Wygant, J. R., Kletzing, C. A., Lessard, M. R., Huang, C., et al. (2015). Van Allen probes, NOAA, GOES, and ground observations of an intense EMIC wave event extending over 12 h in magnetic local time. *Journal of Geophysical Research: Space Physics*, *120*(7), 5465–5488. https://doi.org/10.1002/2015JA021227

Engel, M. A., Morley, S. K., Henderson, M. G., Jordanova, V. K., Woodroffe, J. R., & Mahfuz, R. (2019). Improved simulations of the inner magnetosphere during high geomagnetic activity with the RAM-SCB model. *Journal of Geophysical Research: Space Physics*, *124*(6), 4233–4248. https://doi.org/10.1029/2018JA026260

Funsten, H. O., Skoug, R. M., Guthrie, A. A., MacDonald, E. A., Baldonado, J. R., Harper, R. W., et al. (2013). Helium, oxygen, proton, and electron (HOPE) mass spectrometer for the radiation belt storm probes mission. *Space Science Reviews*, *179*(1–4), 423–484. https://doi.org/10.1007/s11214-013-9968-7

Gkioulidou, M., Ukhorskiy, A. Y., Mitchell, D. G., & Lanzerotti, L. J. (2016). Storm time dynamics of ring current protons: Implications for the long-term energy budget in the inner magnetosphere. *Geophysical Research Letters*, *43*(10), 4736–4744. https://doi.org/10.1002/2016GL068013

Jordanova, V. K., Albert, J., & Miyoshi, Y. (2008). Relativistic electron precipitation by EMIC waves from self-consistent global simulations. *Journal of Geophysical Research*, *113*(A3), A00A10. https://doi.org/10.1029/2008JA013239

Jordanova, V. K., Boonsiriseth, A., Thorne, R. M., & Dotan, Y. (2003). Ring current asymmetry from global simulations using a high-resolution electric field model. *Journal of Geophysical Research*, *108*(A12), 1443. https://doi.org/10.1029/2003JA009993

Jordanova, V. K., Farrugia, C. J., Thorne, R. M., Khazanov, G. V., Reeves, G. D., & Thomsen, M. F. (2001). Modeling ring current proton precipitation by electromagnetic ion cyclotron waves during the May 14–16, 1997, storm. *Journal of Geophysical Research*, *106*(A1), 7–22. https://doi.org/10.1029/2000JA002008

Jordanova, V. K., & Miyoshi, Y. S. (2005). Relativistic model of ring current and radiation belt ions and electrons: Initial results. *Geophysical Research Letters*, *32*(14), L14104. https://doi.org/10.1029/2005GL023020

Jordanova, V. K., Spasojevic, M., & Thomsen, M. F. (2007). Modeling the electromagnetic ion cyclotron wave-induced formation of detached subauroral proton arcs. *Journal of Geophysical Research*, *112*(A8), A08209. https://doi.org/10.1029/2006JA012215

Jordanova, V. K., Tu, W., Chen, Y., Morley, S. K., Panaitescu, A.-D., Reeves, G. D., & Kletzing, C. A. (2016). RAM-SCB simulations of electron transport and plasma wave scattering during the October 2012 "double-dip" storm. *Journal of Geophysical Research: Space Physics*, *121*(9), 8712–8727. https://doi.org/10.1002/2016JA022470

Jordanova, V. K., Zaharia, S., & Welling, D. T. (2010). Comparative study of ring current development using empirical, dipolar, and self-consistent magnetic field simulations. *Journal of Geophysical Research*, *115*(A12), A00J11. https://doi.org/10.1029/2010JA015671

Kersten, T., Horne, R. B., Glauert, S. A., Meredith, N. P., Fraser, B. J., & Grew, R. S. (2014). Electron losses from the radiation belts caused by EMIC waves. *Journal of Geophysical Research: Space Physics*, *119*(11), 8820–8837. https://doi.org/10.1002/2014JA020366

Li, Z., Millan, R. M., Hudson, M. R., Woodger, L. A., Smith, D. M., Chen, Y., et al. (2014). Investigation of EMIC wave scattering as the cause for the BARREL 17 January 2013 relativistic electron precipitation event: A quantitative comparison of simulation with observations. *Geophysical Research Letters*, *41*(24), 8722–8729. https://doi.org/10.1002/2014GL062273

Li, Z.-G., Tu, W., Selesnick, R., & Huang, J. (2024). Modeling the contribution of precipitation loss to a radiation belt electron dropout observed by Van Allen Probes. *Journal of Geophysical Research: Space Physics*, *129*(3), e2023JA032171. https://doi.org/10.1029/2023JA032171

Lyu, X., Jordanova, V. K., Engel, M. A., Tu, W., & Ma, Q. (2024). Quantifying the role of EMIC wave scattering during the 27 February 2014 storm by RAM-SCB simulations [Dataset]. *Zenodo*. https://doi.org/10.5281/zenodo.10775745

Lyu, X., Ma, Q., Tu, W., Li, W., & Capannolo, L. (2022). Modeling the simultaneous dropout of energetic electrons and protons by EMIC wave scattering. *Geophysical Research Letters*, *49*(20), e2022GL101041. https://doi.org/10.1029/2022GL101041

Lyu, X., & Tu, W. (2022). Modeling the dynamics of energetic protons in Earth's inner magnetosphere. *Journal of Geophysical Research: Space Physics*, *127*(3), e2021JA030153. https://doi.org/10.1029/2021JA030153

Lyu, X., Tu, W., Huang, J., Ma, Q., & Li, Z.-G. (2024). Modeling the simultaneous dropout of energetic electrons and protons by magnetopause shadowing. *Geophysical Research Letters*, *51*(2), e2023GL106681. https://doi.org/10.1029/2023GL106681

Ma, Q., Li, W., Thorne, R. M., Ni, B., Kletzing, C. A., Kurth, W. S., et al. (2015). Modeling inward diffusion and slow decay of energetic electrons in the Earth's outer radiation belt. *Geophysical Research Letters*, *42*(4), 987–995. https://doi.org/10.1002/2014GL062977

Ma, Q., Li, W., Yue, C., Thorne, R. M., Bortnik, J., Kletzing, C. A., et al. (2019). Ion heating by electromagnetic ion cyclotron waves and magnetosonic waves in the Earth's inner magnetosphere. *Geophysical Research Letters*, *46*(12), 6258–6267. https://doi.org/10.1029/2019GL083513

Meredith, N. P., Thorne, R. M., Horne, R. B., Summers, D., Fraser, B. J., & Anderson, R. R. (2003). Statistical analysis of relativistic electron energies for cyclotron resonance with EMIC waves observed on CRRES. *Journal of Geophysical Research*, *108*(A6), 1250. https://doi.org/10.1029/2002JA009700

Mitchell, D. G., Lanzerotti, L. J., Kim, C. K., Stokes, M., Ho, G., Cooper, S., et al. (2013). Radiation belt storm probes ion composition experiment (RBSPICE). *Space Science Reviews*, *179*(1–4), 263–308. https://doi.org/10.1007/s11214-013-9965-x

Miyoshi, Y., Sakaguchi, K., Shiokawa, K., Evans, D., Albert, J., Connors, M., & Jordanova, V. (2008). Precipitation of radiation belt electrons by EMIC waves, observed from ground and space. *Geophysical Research Letters*, *35*(23), L23101. https://doi.org/10.1029/2008GL035727

Ni, B., Cao, X., Zou, Z., Zhou, C., Gu, X., Bortnik, J., et al. (2015). Resonant scattering of outer zone relativistic electrons by multiband EMIC waves and resultant electron loss time scales. *Journal of Geophysical Research: Space Physics*, *120*(9), 7357–7373. https://doi.org/10.1002/2015JA021466

Ni, B., Zhang, Y., & Gu, X. (2023). Identification of ring current proton precipitation driven by scattering of electromagnetic ion cyclotron waves. *Fundamental Research*, *3*(2), 257–264. https://doi.org/10.1016/j.fmre.2021.12.018

Olifer, L., Mann, I. R., Ozeke, L. G., Rae, I. J., & Morley, S. K. (2019). On the relative strength of electric and magnetic ULF wave radial diffusion during the March 2015 geomagnetic storm. *Journal of Geophysical Research: Space Physics*, *124*(4), 2569–2587. https://doi.org/10.1029/2018JA026348

Onsager, T. G., Rostoker, G., Kim, H.-J., Reeves, G. D., Obara, T., Singer, H. J., & Smithtro, C. (2002). Radiation belt electron flux dropouts: Local time, radial, and particle-energy dependence. *Journal of Geophysical Research*, *107*(A11), 1382. https://doi.org/10.1029/2001JA000187

Sheeley, B. W., Moldwin, M. B., Rassoul, H. K., & Anderson, R. R. (2001). An empirical plasmasphere and trough density model: CRRES observations. *Journal of Geophysical Research*, *106*(A11), 25631–25641. https://doi.org/10.1029/2000JA000286

Shprits, Y., Drozdov, A., Spasojevic, M., Kellerman, A. C., Usanova, M. E., Engebretson, M. J., et al. (2016). Wave-induced loss of ultra-relativistic electrons in the Van Allen radiation belts. *Nature Communications*, *7*(1), 12883. https://doi.org/10.1038/ncomms12883

Silva, G. B. D., Alves, L. R., Tu, W., Padilha, A. L., Souza, V. M., Li, L.-F., et al. (2022). Modeling radiation belt electron dropouts during moderate geomagnetic storms using radial diffusion coefficients estimated with global MHD simulations. *Journal of Geophysical Research: Space Physics*, *127*(9), e2022JA030602. https://doi.org/10.1029/2022JA030602

Tu, W., Cunningham, G. S., Chen, Y., Morley, S. K., Reeves, G. D., Blake, J. B., et al. (2014). Event-specific chorus wave and electron seed population models in DREAM3D using the Van Allen Probes. *Geophysical Research Letters*, *41*(5), 1359–1366. https://doi.org/10.1002/2013GL058819

Tu, W., Xiang, Z., & Morley, S. K. (2019). Modeling the magnetopause shadowing loss during the June 2015 dropout event. *Geophysical Research Letters*, *46*(16), 9388–9396. https://doi.org/10.1029/2019GL084419

Turner, D. L., Angelopoulos, V., Morley, S. K., Henderson, M. G., Reeves, G. D., Li, W., et al. (2014). On the cause and extent of outer radiation belt losses during the 30 September 2012 dropout event. *Journal of Geophysical Research: Space Physics*, *119*(3), 1530–1540. https://doi.org/10.1002/2013JA019446

Turner, D. L., Shprits, Y., Hartinger, M., & Angelopoulos, V. (2012). Explaining sudden losses of outer radiation belt electrons during geomagnetic storms. *Nature Physics*, *8*(3), 208–212. https://doi.org/10.1038/nphys2185

Usanova, M. E., Mann, I. R., Kale, Z. C., Rae, I. J., Sydora, R. D., Sandanger, M., et al. (2010). Conjugate ground and multisatellite observations of compression-related EMIC Pc1 waves and associated proton precipitation. *Journal of Geophysical Research*, *115*(A7), A07208. https://doi.org/10.1029/2009JA014935

Weimer, D. R. (2005). Improved ionospheric electrodynamic models and application to calculating Joule heating rates. *Journal of Geophysical Research*, *110*(A5), A05306. https://doi.org/10.1029/2004JA010884

Welling, D. T., Jordanova, V. K., Zaharia, S. G., Glocer, A., & Toth, G. (2011). The effects of dynamic ionospheric outflow on the ring current. *Journal of Geophysical Research*, *116*(A2), A00J19. https://doi.org/10.1029/2010JA015642

Xiang, Z., Tu, W., Li, X., Ni, B., Morley, S. K., & Baker, D. N. (2017). Understanding the mechanisms of radiation belt dropouts observed by Van Allen Probes. *Journal of Geophysical Research: Space Physics*, *122*(10), 9858–9879. https://doi.org/10.1002/2017JA024487

Xiang, Z., Tu, W., Ni, B., Henderson, M. G., & Cao, X. (2018). A statistical survey of radiation belt dropouts observed by Van Allen Probes. *Geophysical Research Letters*, *45*(16), 8035–8043. https://doi.org/10.1029/2018GL078907

Yue, C., Li, Y., Kistler, L., Ma, Q., Fu, H., Reeves, G. D., et al. (2023). The densities and compositions of background cold ions based on the Van Allen Probe observations. *Geophysical Research Letters*, *50*(15), e2023GL104282. https://doi.org/10.1029/2023GL104282

Zaharia, S., Jordanova, V. K., Thomsen, M. F., & Reeves, G. D. (2006). Self-consistent modeling of magnetic fields and plasmas in the inner magnetosphere: Application to a geomagnetic storm. *Journal of Geophysical Research*, *111*(A11), A11S14. https://doi.org/10.1029/2006JA011619

Zhang, X.-J., Li, W., Ma, Q., Thorne, R. M., Angelopoulos, V., Bortnik, J., et al. (2016). Direct evidence for EMIC wave scattering of relativistic electrons in space. *Journal of Geophysical Research: Space Physics*, *121*(7), 6620–6631. https://doi.org/10.1002/2016JA022521

Zhang, X.-J., Li, W., Thorne, R. M., Angelopoulos, V., Bortnik, J., Kletzing, C. A., et al. (2016). Statistical distribution of EMIC wave spectra: Observations from Van Allen Probes. *Geophysical Research Letters*, *43*(24), 12348–12355. https://doi.org/10.1002/2016GL071158

Zhao, H., Li, X., Baker, D. N., Claudepierre, S. G., Fennell, J. F., Blake, J. B., et al. (2016). Ring current electron dynamics during geomagnetic storms based on the Van Allen Probes measurements. *Journal of Geophysical Research: Space Physics*, *121*(4), 3333–3346. https://doi.org/10.1002/2016JA022358